Bunk, K., Alencar, I., Morgenroth, W., Bertram, F., Schmidt, C., Zimmer, D., Gruszka, P., Hanefeld, M., Bayarjargal, L., Trautmann, C., Winkler, B. (2021): Surface and subsurface damage in 14 MeV Au ion-irradiated diamond. - Journal of Applied Physics, 130, 10, 105303.

https://doi.org/10.1063/5.0060445

Journal of Applied Physics

Surface and subsurface damage in 14 MeV Au ion-irradiated diamond

Cite as: J. Appl. Phys. **130**, 105303 (2021); https://doi.org/10.1063/5.0060445
Submitted: 18 June 2021 • Accepted: 23 August 2021 • Published Online: 13 September 2021

K. Bunk, I. Alencar, W. Morgenroth, et al.

Journal of Applied Physics ARTICLE scitation.org/journal/jap

Surface and subsurface damage in 14 MeV Au ion-irradiated diamond

Cite as: J. Appl. Phys. **130**, 105303 (2021); doi: 10.1063/5.0060445
Submitted: 18 June 2021 · Accepted: 23 August 2021 ·
Published Online: 13 September 2021

K. Bunk,[1,a)] I. Alencar,[2] W. Morgenroth,[3] F. Bertram,[4] C. Schmidt,[5] D. Zimmer,[6] P. Gruszka,[7] M. Hanefeld,[7] L. Bayarjargal,[1] C. Trautmann,[8,9] and B. Winkler[1]

AFFILIATIONS

[1]Goethe University Frankfurt, Institute of Geosciences, 60438 Frankfurt am Main, Germany
[2]Department of Physics, Federal University of Santa Catarina, CEP 88040-900, Florianópolis, Brazil
[3]Department of Geosciences, University of Potsdam, 14476 Potsdam, Germany
[4]Deutsches Elektronen-Synchrotron DESY, Photon Science, 22607 Hamburg, Germany
[5]Helmholtz Centre Potsdam, GFZ German Research Centre for Geosciences, 14473 Potsdam, Germany
[6]Oxford Instruments GmbH, 65205 Wiesbaden, Germany
[7]Goethe University Frankfurt, Institute of Physics, 60438 Frankfurt am Main, Germany
[8]GSI Helmholtz Center for Heavy Ion Research, 64291 Darmstadt, Germany
[9]Technical University Darmstadt, 64289 Darmstadt, Germany

[a)]**Author to whom correspondence should be addressed:** bunk@kristall.uni-frankfurt.de

ABSTRACT

The effects of ion irradiation on the surface and the subsurface of synthetic diamonds were characterized by using optical microscopy, atomic force microscopy, Raman spectroscopy, x-ray reflectivity, electron backscatter diffraction, and resistivity measurements. Irradiation experiments with 14 MeV Au^{6+} ions with fluences up to 2.4×10^{15} ions/cm^2 were carried out on synthetic single crystal diamonds, grown either at high pressure or by chemical vapor deposition, and on polycrystalline samples with high boron concentrations. We show that the ion irradiation-induced changes to the surface and subsurface of diamonds are rather complex and, especially in the first few nanometers, more severe than generally considered. We establish a model describing the changes in density, defect concentration, topology, crystallinity, and bonding from the surface down to the first few micrometers of the irradiated diamond.

I. INTRODUCTION

Diamonds possess many outstanding properties, such as high thermal conductivity, high resistivity, high breakdown electric field, and relatively high carrier mobility. Diamond is the hardest natural material and is chemically inert. As diamond has a wide bandgap of 5.49 eV, it is optically transparent over a wide spectral range.[1] These specific properties are exploited in numerous applications in science and technology.[2–4] The strong covalent bonding is the origin of high atomic displacement energy which, in conjunction with the low atomic number of carbon, results in diamond being a radiation hard material.[5] This makes diamond suitable as a sensor in radiation detectors.[6,7] For such applications, property changes due to ion irradiation are of interest and numerous studies investigated the radiation damage dot too much a function of ion species, ion energy, and fluence.[8–32] Those studies mainly focused on lower ion energies compared to our experiments or on irradiation with light ions. Here, we report irradiation experiments of diamond with a special focus on analyzing ion beam-induced effects within the first tens of nanometers just below the surface.

When energetic ions penetrate a solid, they are slowed down while depositing energy along their trajectory until they finally come to rest. The energy loss and interaction processes with the target crucially depend on the ion velocity. At high velocities, the ions predominantly interact with the target electrons, causing electronic excitations and ionization of the target atoms (electronic stopping). A few hundred nanometers before the ions are stopped, the energy loss is mainly due to elastic collisions with the target atoms (nuclear stopping).[33,34] Elastic collisions typically produce

Frenkel defects, displaced atoms, and vacancies. The electronic and nuclear energy loss, penetration depths, and defect densities can be obtained with Stopping and Range of Ions in Matter (SRIM) simulations.[35]

Ion irradiation of diamond leads to a breaking of sp^3-bonds and the formation of sp^2-bonds, thus partially graphitizing the lattice.[36] If the defect density exceeds a critical threshold, D_c, an irreversible damage of the irradiated material occurs.[13,21] Irradiations yielding $D_c = 1–9 \times 10^{22}$ vacancies/cm^3 or above will result in an irreversibly graphitized lattice[13,18,21] that cannot be restored to diamond by thermal annealing. For irradiation with doses below D_c, thermal annealing will lead to recrystallization of diamond.[13]

SRIM calculations typically overestimate the vacancy concentration since the model does not account for dynamic annealing, i.e., the recombination of Frenkel pairs in the collision cascade.[37] Computed D_c values thus suffer from systematic errors. Also, damage saturation effects are generally not taken into account.[10,21] The spatial distribution of vacancies obtained from the SRIM calculations can be used to estimate the damage given as displacements per atom, dpa.[38] The dpa gives the average number of displacements experienced by each atom for a given fluence. It, therefore, allows a comparison of damage produced independent of the material and type of irradiation.[38,39]

The production of Frenkel pairs leads to swelling of the crystal. Surface swelling of ion-irradiated diamond is a well-known phenomenon and has been observed for different implantation conditions, including, e.g., 17 MeV F ions (fluences up to 7.6×10^{17} ions/cm^2),[8] He^+ ions (energies from 24 to 350 keV with fluences up to 2.5×10^{17} ions/cm^2),[28] B_2^- ions (60 keV with fluences up to 3×10^{17} ions/cm^2),[40] 1.8 MeV He ions and 2 and 3 MeV H ions (fluences up to 5×10^{17} ions/cm^2),[19] and Au and Br ions (energies from 10 to 40 MeV and fluences up to 5×10^{14} ions/cm^2).[29] It was proposed by Fairchild *et al.*[21] that when reaching D_c, the strain in the diamond exceeds the tensile strength of diamond. They suggest that this causes the lattice to transform into an amorphous phase. A reduction of the density of diamond[41] from 3.5(1) to 3.0(1) g/cm^3 is indicative of reaching D_c.[21] Further damage production decreases the density further, until the density saturates at 2.2(1) g/cm^3. Fairchild *et al.*[21] conclude that damage production in diamond depends on the local density and tensile strain rather than only on the vacancy concentration.

In the present work, we investigated irradiation-induced changes of the surface and the subsurface region of diamonds. Ion-irradiated diamonds were studied by optical microscopy, atomic force microscopy (AFM), Raman spectroscopy, x-ray reflectivity (XRR), and electron backscatter diffraction (EBSD). AFM records the topology and roughness of sample surfaces.[42] Raman spectroscopy is based on the inelastic scattering of photons by phonons and is a commonly employed technique to characterize carbon materials.[43] It provides information about bonding and can be utilized to detect radiation-induced modifications of the lattice. XRR is a non-destructive technique where the reflectivity of x-rays close to the glancing angle is determined. The dependence of the scattered x-rays as a function of the incident angle allows the characterization of the subsurface structure of a material in terms of the internal layering, layer thickness and density, as well as surface and interfacial roughness.[44] EBSD provides information about the structure.[45] Further measurements were carried out to determine the electrical resistivity of the ion-irradiated samples.

II. METHODS

A. Samples

We irradiated synthetic single crystal and polycrystalline diamond plates obtained from Element Six.[46] The samples were synthesized either by chemical vapor deposition (CVD) or by the High Pressure High Temperature (HPHT) method.[47] The sample characteristics are listed in Table I. The single crystals are (100) plates. All samples had a polished surface, except for sample EP Poly, which has an as-grown surface. The nominal roughnesses provided by the manufacturer are given in Table I. Sample EP Poly is boron doped. It has a resistivity of 0.02(3)–0.18(3) Ω cm.[46] Photographs of the four different samples are shown in Fig. 1.

B. Ion irradiation

The samples were irradiated with 14 MeV Au^{6+} ions at the 3 MV tandetron accelerator at the Ion Implantation Laboratory at the Federal University of Rio Grande do Sul, Porto Alegre, Brazil. The selection of Au ions was motivated by the fact that due to the high atomic number of Au, the energy deposited in the sample is large (Fig. 2). The ion beam had a spot size of few millimeters and was scanned over a 2×2 cm^2 area. During the irradiation, the samples were placed behind a 2 mm thick steel mask with circular apertures of 2 mm in diameter. This led to 2 mm diameter irradiated spots on the samples surrounded by pristine material and allowed us to directly compare the physical and optical properties of the pristine and irradiated sample area. Samples of each type were irradiated with fluences of 5.3×10^{14}, 1.8×10^{15}, and 2.4×10^{15} ions/cm^2 to generate different levels of lattice damage. The irradiation was carried out under normal beam incidence and at ambient temperature.

TABLE I. Properties of the diamond samples used for the experiments according to the manufacturer.

Sample name	Synthesis method	Dimensions (mm)	B content (ppm)	N content (ppm)	Roughness (nm)	Sample type
SC CVD	CVD	$3 \times 3 \times 0.3$	<0.05	<1	<30	Single crystal IIa
SC Ib	HPHT	$3 \times 3 \times 0.3$	<0.1	<200	<30	Single crystal Ib
TM 100	CVD	$10 \times 10 \times 0.5$	<0.0005	<0.05	<50	Polycrystalline
EP Poly	CVD	$5 \times 5 \times 0.45$	1100–4500	<0.05	≈50 000	Polycrystalline

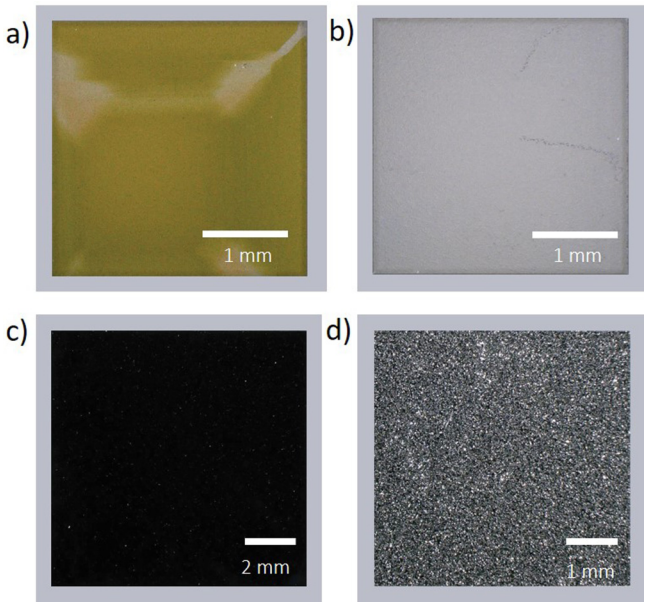

FIG. 1. Photographs of the single crystal samples (a) SC Ib and (b) SC CVD and polycrystalline samples (c) TM 100 and (d) EP Poly. Images were taken in the reflected light mode. The irregular color of sample SC Ib is indicative of an inhomogeneous distribution of nitrogen in the sample.

C. SRIM calculations

Calculations of the energy loss, ion range, and defect concentration were performed with SRIM-2013.[48,49] The electronic and nuclear energy losses of 14 MeV Au ions in a carbon target with a density of 3.5 g/cm^3 are given in Fig. 2. At the sample surface, the electronic stopping is 6.1 keV/nm and the nuclear stopping is 1.6 keV/nm. The 14 MeV Au ions are stopped at about 1.75 μm in the diamond. The simulation was run in the "Quick Kinchin and Pease mode" with a displacement energy of 37.5 eV.[50] Figure 3(a) gives the vacancy density as a function of sample depth for the three different fluences we studied. As mentioned above these simulations only give an estimate of the damage. The maximum values are 8.55×10^{22}, 2.9×10^{23}, and 3.87×10^{23} vacancies/cm^3 for the three different fluences (5.3×10^{14}, 1.8×10^{15}, and 2.4×10^{15} ions/cm^2). The displacements per atom are given in Fig. 3(b).

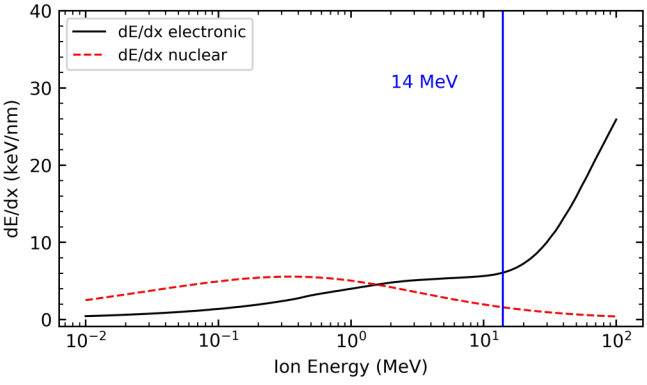

FIG. 2. Electronic and nuclear stopping for Au ions in carbon (density of 3.5 g/cm^3) as a function of ion energy, calculated with SRIM-2013.[48]

D. Optical microscopy

Optical microscopy was performed with a Keyence digital microscope VHX-6000. The microscope allows observation in transmitted and reflected light. Topographic information can be obtained by the Depth from Defocus method, where images from different focus levels are combined to form 3D images.

E. AFM measurements and swelling

Atomic force microscopy (AFM) allows the direct imaging of samples surfaces. The spatial resolution in the vertical direction is in the sub-nanometer range, while an in-plane resolution of several tens of nanometers can be achieved.[42]

AFM measurements were carried out using the dynamic force mode with a Nanosurf Easyscan 2 AFM. Using a piezoelectric actuator, the AFM cantilever is vibrating perpendicular to the sample surface near its resonance frequency. A change of the cantilevers oscillation amplitude occurs when the tip interacts with the surface.[51]

A survey measurement was carried out with a scan size of $50 \times 50\,\mu$m^2. From this scan, an area of $1 \times 1\,\mu$m^2 was selected. Roughness values were obtained from both measurements. Measurements were carried out along 256 lines with scan times of 1 s per line. For the data analysis, the program Gwyddion[52] was used. The root mean square roughness, R_q, was determined, which is given by

$$R_q = \sqrt{\frac{1}{N}\sum_{j=1}^{N} r_j^2}, \tag{1}$$

where N is the number of data points along the evaluation length and r the measured height deviations from the mean height.

F. Electrical resistivity measurements

Resistivity measurements were carried out by applying the four-probe method[53] and using a Keithley DMM7510 digital multimeter. The irradiated areas of the single crystal samples Ib and CVD and the polycrystalline sample TM 100 irradiated with low fluence (5.3×10^{14} ions/cm^2) and high fluence (2.4×10^{15} ions/cm^2) were measured. Additionally, a pristine sample of the boron-doped polycrystalline diamond EP Poly was measured to benchmark the measurement method.

G. Raman spectroscopy

Raman spectroscopy was carried out with a HORIBA Jobin Yvon LabRAM HR800 VIS with an excitation wavelength of $\lambda = 532$ nm. Additional measurements were carried out with a custom setup in Frankfurt as described in detail in Bayarjargal *et al.*[54]

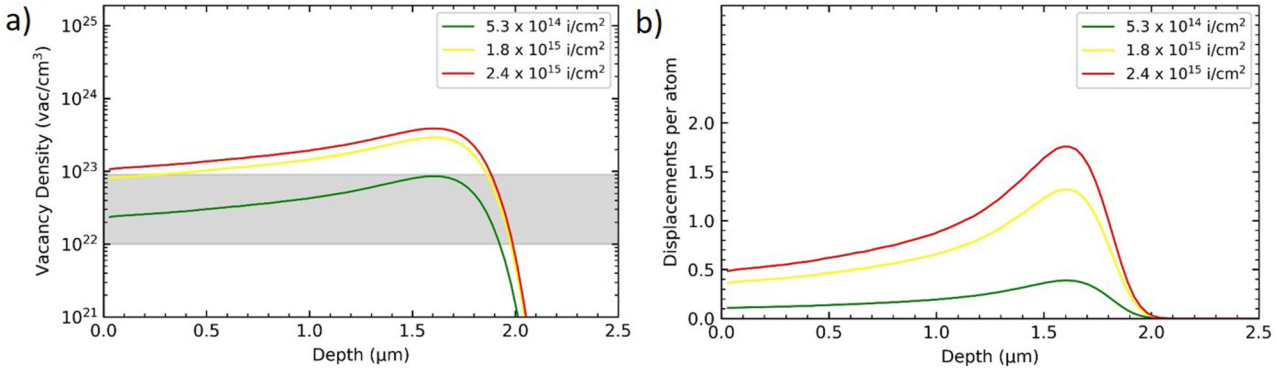

FIG. 3. Depth profiles of (a) the defect density (vacancies) and (b) displacements per atoms obtained by SRIM-2013[48] for 14 MeV Au ions impinging on diamond for the fluences accumulated in our experiments. The horizontal shaded band in (a) shows the critical density of defects, D_c, at which an irreversible graphitization occurs.[21]

We used an OXXIUS S.A. Laser-Boxx LMX532 laser ($\lambda = 532$ nm) and a Princeton Instruments ACTON SpectraPro 2300i spectrograph equipped with a Pixis256E CCD camera.

H. Density functional theory calculations

First-principles calculations were carried out within the framework of density functional theory (DFT),[55] employing the Perdew–Burke–Ernzerhof (PBE) exchange-correlation function[56] and the plane wave/pseudopotential approach implemented in the CASTEP[57] simulation package. "On the fly" norm-conserving or ultrasoft pseudopotentials generated using the descriptors in the CASTEP database were employed in conjunction with plane waves up to a kinetic energy cutoff of 990 or 630 eV, for norm-conserving and ultrasoft pseudopotentials, respectively. The accuracy of the pseudopotentials is well established.[58] A Monkhorst–Pack[59] grid was used for Brillouin-zone integrations with a distance of < 0.023 Å^{-1} between grid points. Convergence criteria included an energy change of $< 5 \times 10^{-6}$ eV atom^{-1}, a maximal force of < 0.008 eV/Å, and a maximal component of the stress tensor < 0.02 GPa. Phonon frequencies were obtained from density functional perturbation theory (DFPT) calculations. Raman intensities were computed using DFPT with the "$2n + 1$" theorem approach.[60]

I. X-ray reflectivity

The refractive index of x-rays in solids is slightly less than unity, hence x-rays undergo total reflection for incident angles smaller than the critical angle for total reflection, θ_c. For angles above θ_c, the interior structure of a sample is probed and the reflectivity of the x-rays decreases rapidly.[44] For layers deposited on a substrate, interferences occur between the x-rays reflected from different layers and the interfaces between them. The reflectivity profiles then show oscillations, referred to as "Kiessig fringes." It was shown by Kiessig[61] that the reflection and transmission of x-rays can be described by the Fresnel equation and that their reflection can be treated exactly like the reflection of visible light in the kinematic approximation. The critical angle for θ_c for total reflection is given by[44]

$$\theta_c = \sqrt{2\delta(\lambda)}, \tag{2}$$

with the wavelength dependent dispersion $\delta(\lambda)$,

$$\delta(\lambda) = \frac{r_e \lambda^2}{2\pi} \rho \frac{\sum_k [f_k^0(\lambda) + f_k'(\lambda)]}{\sum_k M_k}, \tag{3}$$

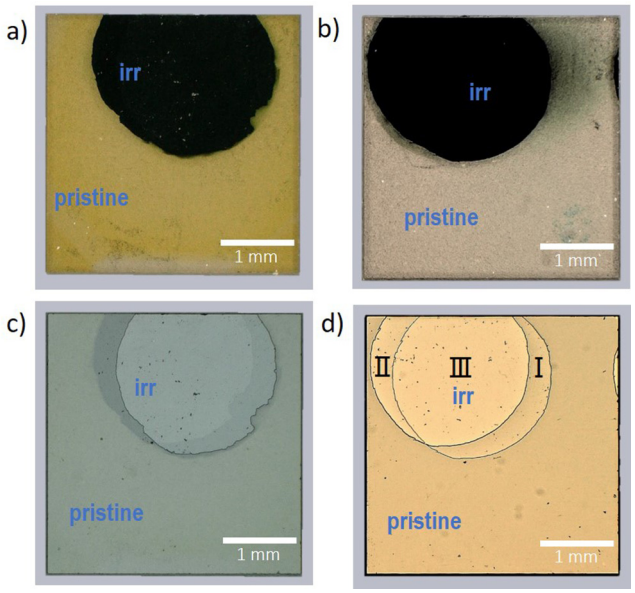

FIG. 4. Optical microscopy images of the single crystal samples after irradiation. Images were taken for SC Ib (a) and (c) and SC CVD (b) and (d) in the reflected light mode. As the steel mask was shifted once during irradiation, there are three distinct areas, which were irradiated with fluences of 5.3×10^{14}, 1.8×10^{15}, and 2.4×10^{15} ions/cm^2 and are labeled with I, II, and III, respectively.

with r_e being electron radius (2.818×10^{-15} m), λ being x-ray wavelength, ρ being density, M_k being atomic mass, f_k^0 being non-resonant term of the atomic scattering factor, and f_k' being dispersion correction.

Equation (3) shows that δ and, therefore, θ_c depends on the x-ray wavelength, the density, and the composition of the material. For specular reflection, the incident angle θ_i and exit angle θ_f are equal. Then, the momentum transfer $\vec{q} = \vec{k_f} - \vec{k_i}$ is along the surface normal (z direction). Depending on the x-ray wavelength λ, the momentum transfer is

$$q_z = \frac{4\pi}{\lambda} \sin\theta_i. \tag{4}$$

X-ray reflectivity (XRR) measurements were performed at the PETRA III/DESY beamline P08 using a photon energy of 10 keV. The critical angle for total reflection [Eq. (2)] for diamond at 10 keV is 0.22°. The beam had a size of $2.5 \times 30\,\mu m^2$ (h × v) resulting in a footprint on the sample of $0.7 \times 0.03\,mm^2$. The reflected intensity was measured as a function of the grazing-incidence angle for the pristine and irradiated part of each sample. XRR data were obtained for the single crystal diamond samples irradiated with 5.3×10^{14} and 2.4×10^{15} ions/cm^2. The XRR data were analyzed using the software REFLEX[62] employing the matrix formalism[44] and a Nelder–Mead (NM) simplex optimization algorithm.[63] The free parameters used for the fit were electron densities, surface and interfacial roughnesses, and layer thicknesses.

J. Electron backscatter diffraction

Electron backscatter diffraction is usually carried out using a scanning electron microscope (SEM) equipped with an EBSD camera. The samples are tilted toward the diffraction camera.

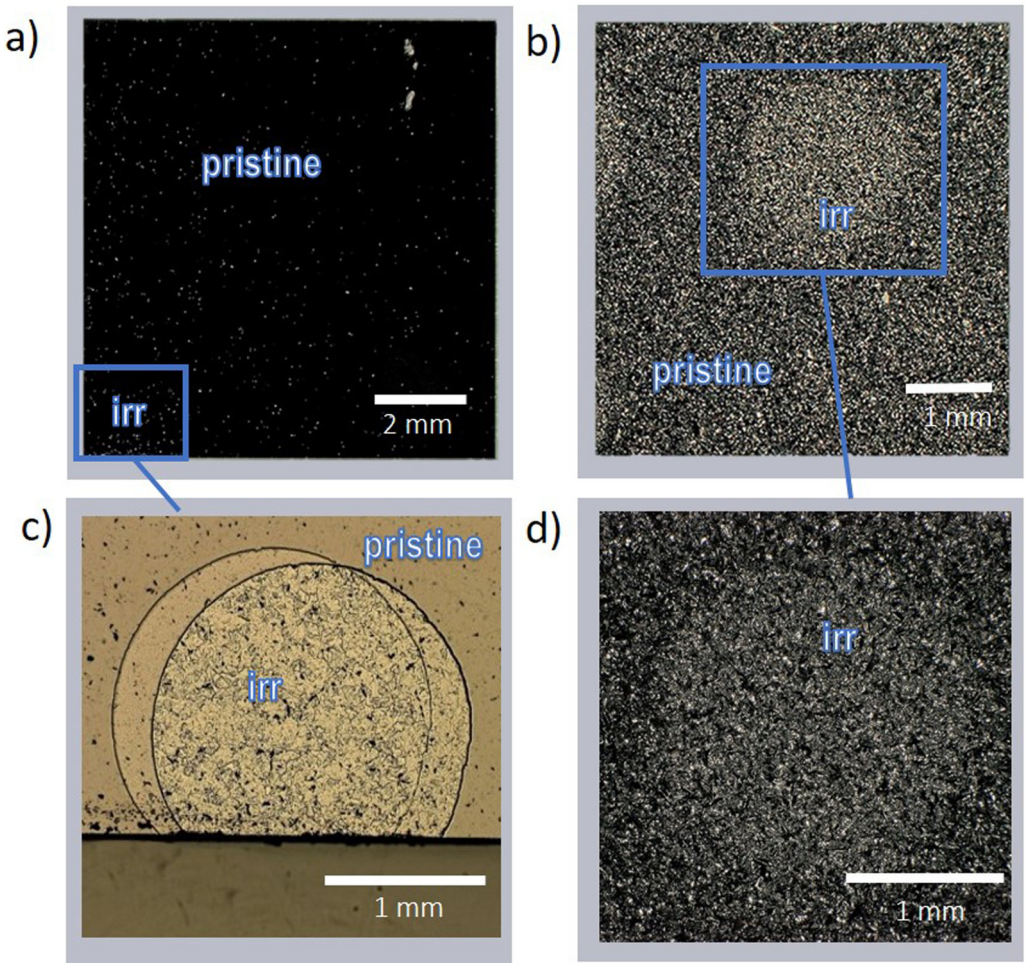

FIG. 5. Optical microscopy images of the polycrystalline samples after irradiation. Images were taken for sample TM 100 (a) and (c) and sample EP Poly (b) and (d) in the reflected light mode. Magnified areas in (c) and (d) are indicated in (a) and (b).

Electrons backscattered from the sample may exit near the Bragg angle-forming Kikuchi bands. Those bands correspond to the lattice planes of the crystal structure and can be indexed accordingly. Thus, the crystal symmetry and orientation of the material can be determined.[64] Electron backscatter diffraction was carried out on a Carl Zeiss GeminiSEM 450 field emission electron microscope equipped with the Oxford Instruments CMOS EBSD Camera Symmetry (Oxford Instruments GmbH, Wiesbaden). Measurements were performed using an acceleration voltage of 10 kV and a beam current of 500 pA at a working distance of 14 mm. The sample was tilted by 70° with respect to the electron beam. Electron backscatter patterns were collected with an exposure time of 29 ms and a frame averaging of 10. Data acquisition and indexing were performed with AZtec 5.0.[65]

III. RESULTS

A. Optical microscopy

Optical microscopy images of the single crystal samples are shown in Fig. 4. The images were taken in the reflected light mode and show that the formerly transparent single crystal samples darkened in the irradiated areas. The images in Figs. 4(c) and 4(d) show clearly the demarcation between the irradiated areas and the remaining pristine diamond. During the irradiation, the samples were once slightly shifted with respect to the steel mask. The effect of this shift is clearly observable.

The polycrystalline samples also show surface alterations (Fig. 5), which are most obvious for sample TM 100 [Fig. 5(c)]. For sample EP Poly [Fig. 5(d)], the damage is difficult to visualize by optical microscopy.

Reconstructions of the topography of the samples from focus stacking are shown for samples SC Ib and SC CVD in Fig. 6. The irradiated parts of the samples clearly show swelling, but as the AFM measurements discussed below provide a more accurate determination of the step height, no attempt was made to determine the step height quantitatively here.

B. AFM measurements

1. Swelling

We assessed the swelling of the irradiated volume with AFM by measuring the step height of the rims of the irradiated areas (Fig. 7).

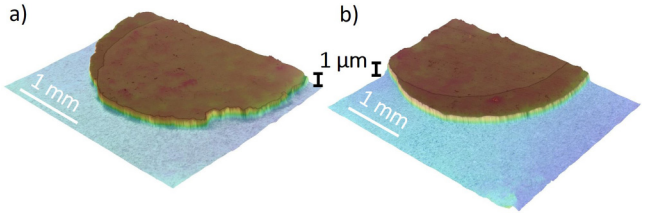

FIG. 6. 3D topography reconstructed from optical microscopy focus stacking of samples SC Ib (a) and SC CVD (b). The irradiated parts of the samples show a significant height difference compared to the pristine areas. The vertical scale is transferred from AFM measurements.

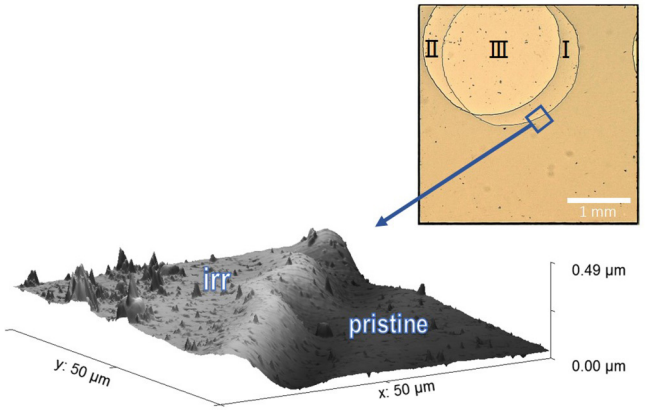

FIG. 7. AFM scan over the rim between pristine and low fluence irradiated (5.3×10^{14} ions/cm^2) area in a single crystal diamond (SC CVD). The location of the scanned area is indicated in the optical micrograph of the sample (right top).

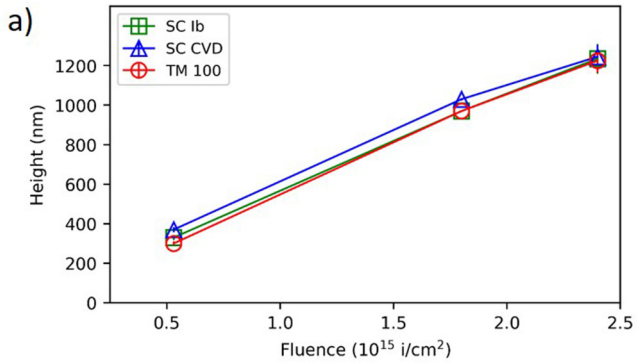

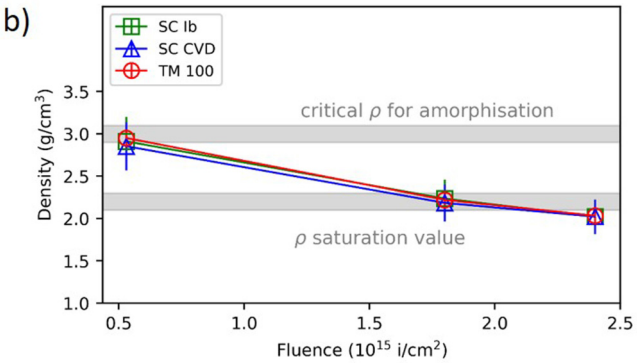

FIG. 8. Step height of swelling measured by AFM (a) and calculated density (b) as a function of fluence. The value for the critical density for amorphization and the density saturation by Fairchild *et al.*[21] are indicated in (b). The error bars are within the data points for (a).

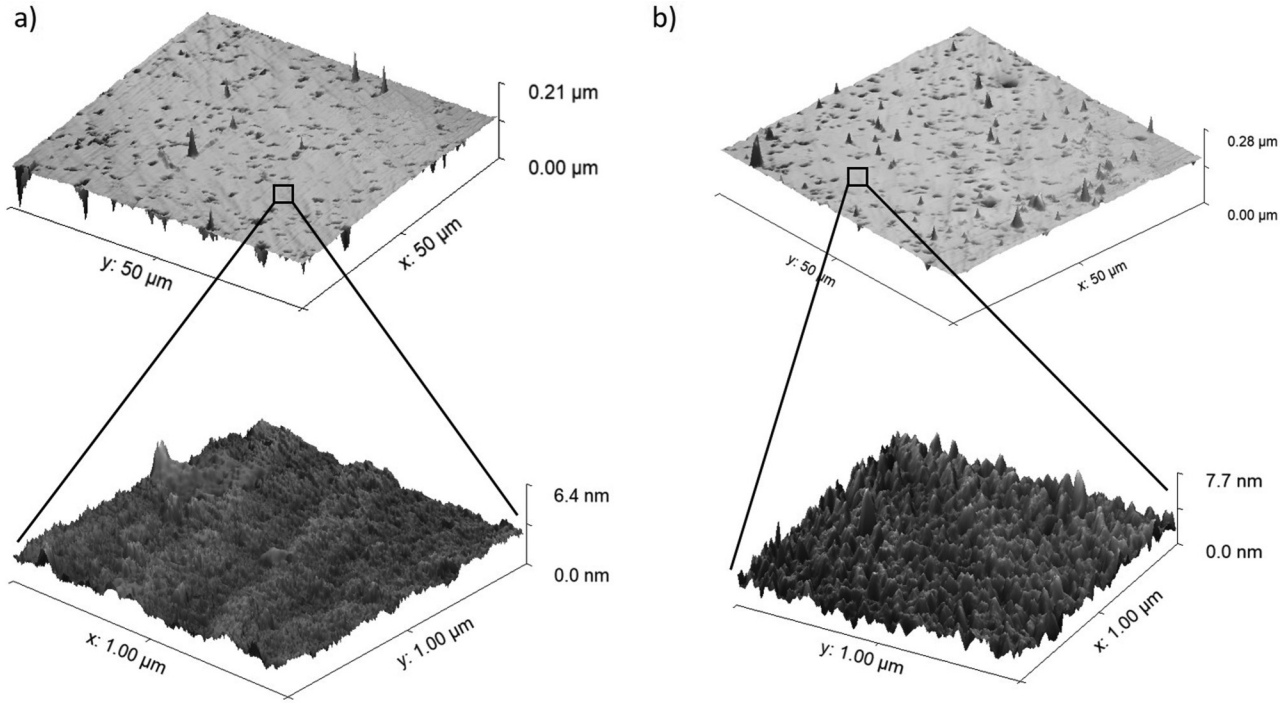

FIG. 9. AFM measurements of the pristine (a) and irradiated (b) single crystal diamond sample (SC CVD) (fluence of 2.4×10^{15} ions/cm^2). Scan of $50 \times 50\,\mu$m^2 (upper scans) and scan of $1 \times 1\,\mu$m^2 (lower scans).

The samples show an increasing swelling with increasing fluence. The step height and corresponding density for the single crystal samples and the polycrystalline sample TM 100 are given in Fig. 8. The surface of the polycrystalline sample EP Poly could not be characterized with AFM due to its roughness. The density was computed by assuming a uniform expansion in the cylindrical irradiated volume, where the lateral dimension of the latter corresponds to the diameter of the mask, while the height of the cylinder is given by the range of the Au ions in diamond derived from the SRIM calculations. Within the experimental error, the swelling of the three tested samples is the same and independent from the type of sample (HPHT synthesized single crystal, CVD-grown single crystal, or polycrystalline).

2. Roughness

AFM was further carried out to measure the roughness and surface texture for the pristine and irradiated parts of the single crystal samples. AFM scans of a pristine and irradiated single crystal diamond of type CVD diamond are shown in Fig. 9.

The AFM scans of the irradiated parts gave no indication of surface contamination during the irradiation process, i.e., we did not observe any hillocks or other unexpected features. The surface roughness of all samples is summarized in Table II. Within the experimental error, the pristine samples have the same surface roughness of 4–5 nm. The results obtained from the scans over the very small areas of $1 \times 1\,\mu$m^2 are not representative as very smooth areas had been chosen from the survey scans for these measurements. The values obtained from the scans over the $50 \times 50\,\mu$m^2 provide more robust data.

C. Electrical resistivity measurements

In order to perform four-terminal sensing, copper electrodes were attached to the samples (Fig. 10). Conductive silver paint was used to connect the electrodes to the irradiated areas [Fig. 10(a)]. For the pristine single crystal diamonds and polycrystalline

TABLE II. Surface roughness for the pristine samples and the samples irradiated with low fluence (5.3×10^{14} ions/cm^2) and high fluence (2.4×10^{15} ions/cm^2) determined for different areas ($50 \times 50\,\mu$m^2 and $1 \times 1\,\mu$m^2) measured by AFM. The manufacturer's specification for the roughness is <30 nm.

		Roughness σ (nm)		
Sample	Area (μm^2)	Pristine	Low fluence	High fluence
SC Ib	50×50	5(1)	15(5)	9(5)
SC Ib	1×1	0.5(5)	0.9(4)	0.7(3)
SC CVD	50×50	4(2)	12(5)	7(5)
SC CVD	1×1	0.5(5)	0.4(4)	0.7(3)

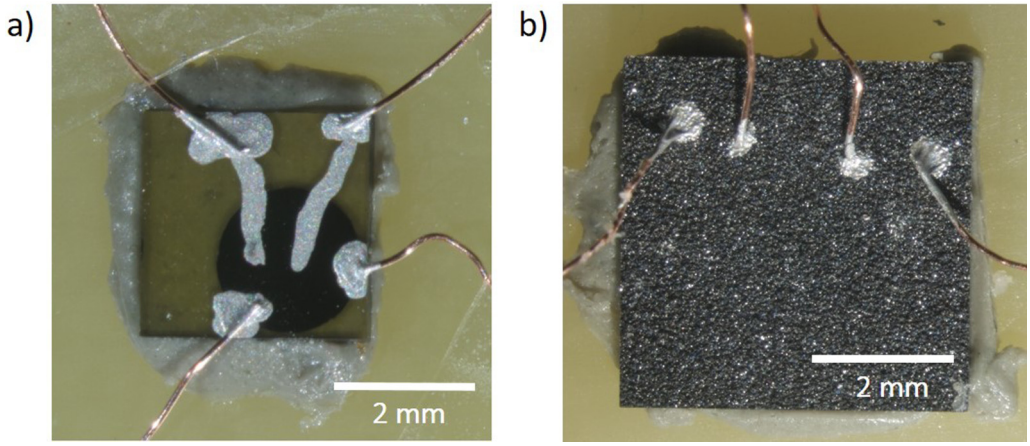

FIG. 10. Images of the single crystal sample Ib (low fluence sample) (a) and pristine sample EP Poly (b) with the electrodes attached for resistivity measurements.

diamonds TM 100, the electrical resistivity could not be determined because of the high resistivity of diamond of $10^{20}\,\Omega\,\mathrm{cm}$.[41]

The electrical resistivity of the boron-doped pristine EP Poly was found to be in excellent agreement with the specifications of the manufacturer Element Six [0.02(3)–0.18(3) Ω cm]. The values obtained for the irradiated parts of the samples are given in Table III.

Vance *et al.*[66] measured the electrical resistivity of neutron-irradiated diamonds as a function of the relative density reduction $\Delta\rho/\rho_0$ due to irradiation. Their results are given, together with our data and the specifications of Element Six, for sample EP Poly in Fig. 11. $\Delta\rho/\rho_0$ is the density decrease obtained from swelling (see Sec. III B 1).

D. Raman spectroscopy

1. Pristine samples

Raman spectroscopy was carried out on the pristine parts of the diamond samples, and the corresponding spectra are shown in Fig. 12. The narrow first-order diamond band at $1334(2)\,\mathrm{cm}^{-1}$ with F_{2g}-symmetry is observed for all pristine samples. For the HPHT single crystal SC Ib, it is the only mode observed in the spectral range investigated here. In the spectrum of the CVD-grown single crystal SC CVD, there is a very weak broad maximum at $1432\,\mathrm{cm}^{-1}$, which is probably due to hydrogen containing defects in the lattice or on the surface. In the polcrystalline samples TM100 and EP Poly, the "G-band," centered at around $1538\,\mathrm{cm}^{-1}$ with a Full Width Half Maximum (FWHM) of $81\,\mathrm{cm}^{-1}$ can be attributed to graphitic assemblages at grain boundaries.[43] This is also the origin of the broad (FWHM of $83\,\mathrm{cm}^{-1}$), Gaussian-shaped "D-band," centered at $1337\,\mathrm{cm}^{-1}$, on which the narrow diamond line is superposed in the polycrystalline TM 100 sample. Raman spectra of the pristine polycrystalline sample EP Poly is typical for that of a boron-doped diamond.[67] At low energies, a very high background is characteristic, which decreases with increasing energy and contains several weak broad maxima, e.g., at around $500\,\mathrm{cm}^{-1}$, labeled B1 in Fig. 12. The additional maxima in

TABLE III. Electrical resistivities obtained for the samples irradiated with low fluence (5.3×10^{14} ions/cm^2) and high fluence (2.4×10^{15} ions/cm^2).

	Resistivity (Ω cm)	
Sample	Low fluence	High fluence
SC Ib	57(7)	0.6(2)
SC CVD	8(3)	0.5(2)
TM 100	$3(1) \times 10^5$	0.5(2)

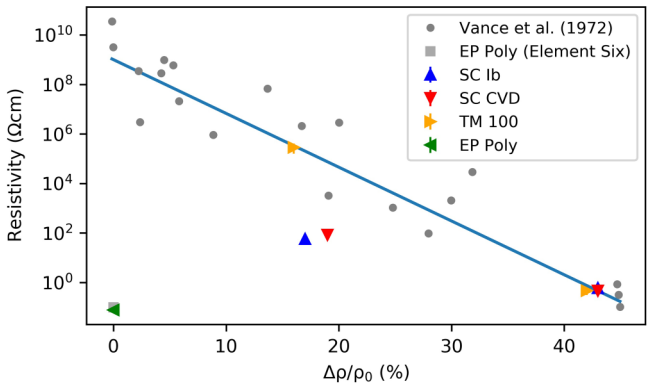

FIG. 11. Resistivity of irradiated diamonds as a function of relative density decrease due to irradiation. Data from Vance *et al.*[66] for neutron-irradiated diamonds (grey circles) are shown together with data for ion-irradiated diamonds of type SC Ib, SC CVD, and TM 100 (this work). The measured resistivity of the pristine sample EP Poly is given together with specifications of the manufacturer Element Six (gray square). The resistivity decreases exponentially with the relative density change (straight line). The error bars are within the data points.

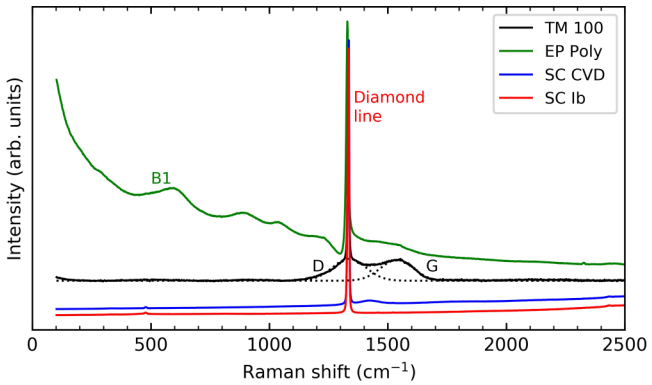

FIG. 12. Raman spectra of pristine single crystal diamond samples SC Ib and SC CVD, polycrystalline diamond samples TM 100, and boron-doped polycrystalline samples EP Poly. The dashed lines represent two Gaussians fitted to the data to determine the position and FWHM of the D- and G-bands.

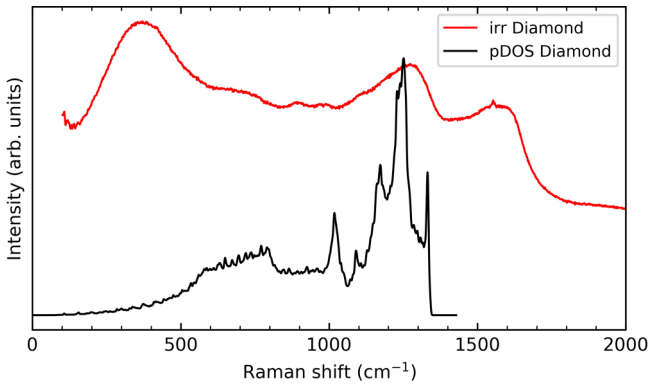

FIG. 14. Comparison of the phonon density of states (pDOS) of diamond computed by DFPT with the experimentally determined Raman spectrum of high fluence (2.4×10^{15} ions/cm^2) irradiated diamond SC Ib. The broad maxima in the Raman spectra, which coincide with maxima in the pDOS may be due to a relaxation of selection rules due to damage to the lattice.

the boron-doped samples are due to local disturbances in the translational symmetry by the defects, which cause the selection rules to be relaxed. In such cases, Raman scattering can occur for phonons, which would be inaccessible in an ordered ideal lattice and is most likely to occur at those frequencies where the phonon density of states (pDOS) has maxima.[67]

2. Irradiated samples

Spectra obtained from the irradiated diamond sample SC Ib are shown for the different fluences as colored lines in Fig. 13.

The spectra are rather similar, i.e., they do not depend significantly on the fluence applied. No difference for the various samples is observed. The three broad maxima are centered at ≈380, ≈1250, and ≈1630 cm^{-1} (marked as I, II, and III in Fig. 13). Weaker spectral features, such as those observed in the pristine samples due to boron doping, are not readily observable anymore.

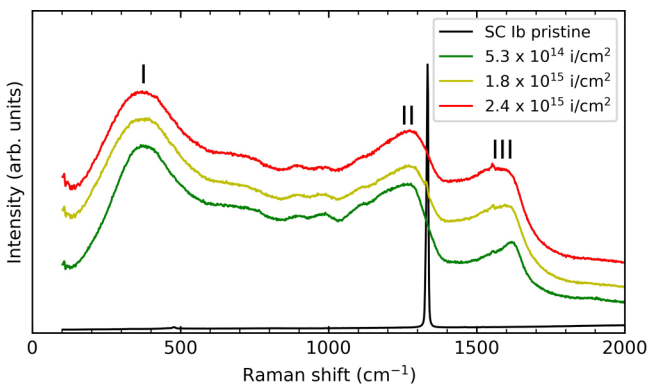

FIG. 13. Stacked Raman spectra of pristine (black line) and irradiated (colored lines) single crystal diamonds SC Ib.

It has been discussed that irradiation-induced defects lead to a relaxation of the selection rules (e.g., Khomich *et al.*[68]), and then, the pDOS can partially be probed by Raman spectroscopy. Figure 14 shows a superposition of a theoretical pDOS obtained for diamond and a Raman spectrum obtained from an irradiated sample.

In order to achieve a more quantitative description of the change in the spectra due to irradiation, the two broad maxima in the region of 1000–1700 cm^{-1} were decomposed into Gaussians, on the assumption that the underlying spectral features have a frequency distribution due to a distribution of local atomic arrangements. Typical fits are shown in Fig. 15, and the peak positions of the Gaussian curves fitted to the maxima II and III for all samples as a function of fluence are shown in Fig. 16. For all samples, the band positions shift slightly for the different fluences. The band at ≈1540 cm^{-1} shows significant shifts to higher wavenumbers for all

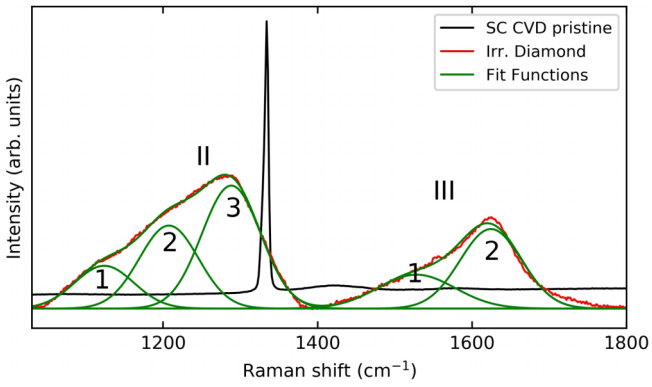

FIG. 15. Raman spectra of pristine (black line) and single crystal sample SC CVD irradiated with 5.3×10^{14} ions/cm^2 (low fluence). The broad maxima II and III were fitted with three and two Gaussian contributions, respectively.

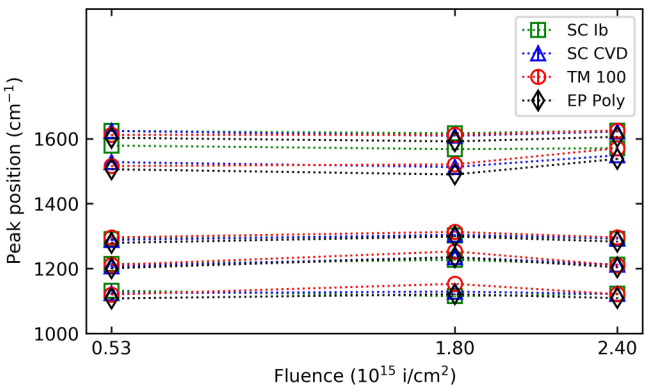

FIG. 16. Peak positions of the Gaussian curves fitted to the maxima II and III of Raman spectra obtained for the irradiated diamond samples as a function of fluence. The error bars are within the data points.

the samples. The background subtracted spectra of the pristine sample SC CVD (black line) are also shown as a reference in Fig. 15. The diamond line of the pristine sample has a FWHM of 6(1) cm^{-1}.

E. X-ray reflectivity

1. Pristine samples

The wave vector dependencies of the experimentally determined XRR intensities of the pristine diamonds show the expected monotonous decrease of the reflectivity for angles above the critical angle for total reflection θ_c (Fig. 17). In the graph, the absolute reflectivity for sample SC Ib is plotted as a function of the momentum transfer vector, where $q_z = 4\pi \sin\theta/\lambda$, with $\lambda = 0.12$ nm. The results of a model fit (see Section II I) are superposed on the measured data in Fig. 17, and the parameters for the roughness and electron density for the single crystal samples are listed in Table IV.

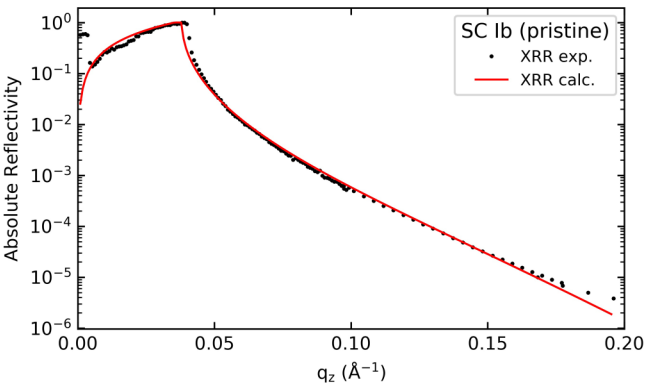

FIG. 17. Intensity as a function of momentum transfer vector q_z for the experimental and calculated data of the pristine diamond sample SC Ib. The parameters obtained by fitting are reported in Table IV.

TABLE IV. Summary of XRR parameters for the pristine single crystal diamond samples obtained from fitting.

Sample	Roughness σ (nm)	Electron density ρ_e (e^-/Å^3)
SC Ib	1.1(2)	1.03(5)
SC CVD	1.1(2)	1.08(5)

The model describes the observed decrease of the intensity over five orders of magnitude very well. For all pristine samples, the fits yield the expected electron density of diamond [≈1.1(1) e$^-$/Å^3], which corresponds to a mass density of 3.5(2) g/cm^3.

2. Irradiated samples

The XRR data obtained from irradiated areas exhibit well-defined Kiessig fringes[61] (Fig. 18). The experimental data can, in all cases, be satisfactorily described by assuming the formation of either two (low fluence) or three (high fluence) layers on top of diamond. The thicknesses of the layers, their electron density and roughness were obtained from a numerical fit (see Section II I) and are listed in Table V.

The XRR data from diamonds irradiated with the lower fluence of 5.3×10^{14} ions/cm^2 can be described by a model consisting of an Ångstrom thick surface layer, followed by a 4–5 nm thick modified layer on top of the diamond (Fig. 19). Based on the numerical fit, the surface layer has an electron density of 0.16(5) e^-/Å^3. The layer underneath (Layer 1) has an electron density of 0.82(5) e^-/Å^3. Fitting the XRR data of both samples independently, we obtain a very similar parameter set (layer thickness, roughness, and electron density) for the low-density layers (Table V). This implies that the surface modification due to ion irradiation is independent of whether a single crystal diamond has been grown at HPHT or by CVD.

The scattered intensity from samples irradiated with a higher fluence (2.4×10^{15} ions/cm^2) needs to be described with three layers on top of diamond (Fig. 20) in order to achieve a satisfactory match of the experimental data. Again the uppermost surface is modeled by a very thin layer with an electron density of 0.16(5)e^-/Å^3. The two layers underneath show decreasing electron densities toward the surface, with ≈1.0(1) e^-/Å^3 (Layer 1) and ≈0.6(2) e^-/Å^3 (Layer 2).

The models for the low fluence samples with one layer and a surface layer were fitted with eight parameters. The models with two layers and a surface layer on top of the diamond were fitted with 11 parameters. The numerical fit is robust in the sense that any model with one parameter less yields a substantially poorer description of the experimental data. The numerical errors are given in Table V. The set of parameters obtained by fitting the XRR data of the two high fluence samples differ more than the set of parameters for the low fluence samples but clearly show that the structural changes induced by high fluence irradiation are qualitatively different from those at low fluences (Table V).

F. Electron backscatter diffraction

EBSD measurements were carried out on the pristine and irradiated areas of the sample SC Ib (Fig. 21). The patterns were

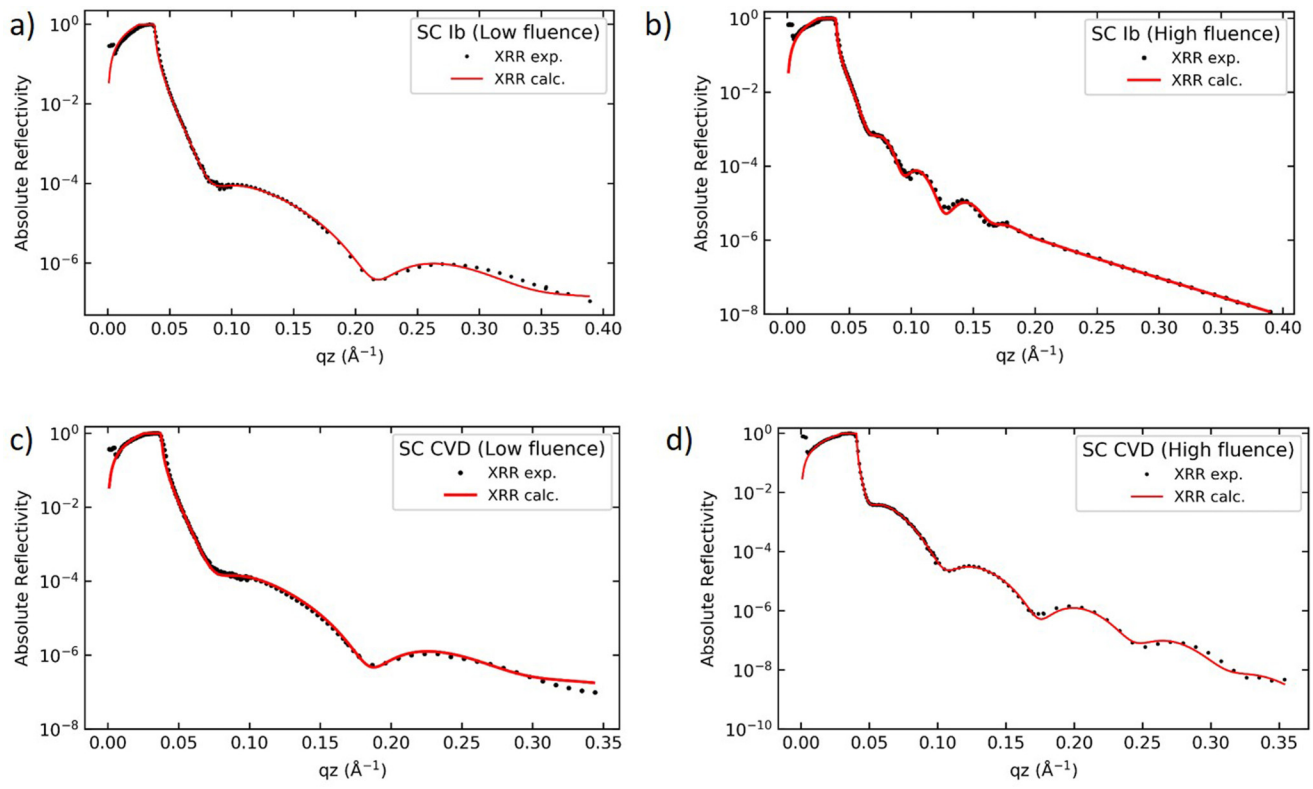

FIG. 18. Intensity as a function of momentum transfer vector q_z for the experimental and calculated data of the diamond samples Ib and CVD irradiated with 5.3×10^{14} ions/cm^2 (low fluence samples) (a) and (c) and 2.4×10^{15} ions/cm^2 (high fluence samples) (b) and (d). The parameters obtained from fitting are reported in Table V.

successfully indexed based on the crystal structure of diamond [space group: $Fd\bar{3}m$ (Int. Table 227), lattice parameter $a = 3.54$ Å] using 11 Kikuchi bands, a Hough-space resolution of 95 and 41 reflectors. The mean angular deviation (MAD) between the detected bands and the theoretical model for the pristine, the low irradiated and the high irradiated region were found to be 0.17° (a), 0.23° (b), and 0.36° (c), respectively (Fig. 21). The sharp and well-defined bands for the pristine sample are indicative of the high quality of the sample. With increasing irradiation, the Kikuchi patterns become increasingly blurred. The information depth of backscattered diffracted electrons is a few tens of nanometers.[69] Hence, these measurements show a degradation of the crystallinity at and directly below the surface.

IV. DISCUSSION

The transformation from transparent single crystal samples to dark samples due to irradiation is the first evidence for the expected formation of sp^2-bonded carbon. According to the SRIM calculations, the graphitization threshold D_c between 1 and 9×10^{22} vacancies/cm^3 was reached or surpassed for all fluences. We observed swelling for the irradiated areas. The step height of the swollen areas was measured with AFM. The densities estimated from the swelling for the different fluences are close to or slightly less than the value for the critical density for amorphization proposed by Fairchild *et al.*[21] [3.0(1) g/cm^3]. This is consistent with the density of defects obtained from SRIM calculations. For the samples exposed to the highest fluence, the density saturation value proposed by Fairchild *et al.*[21] [2.2(1) g/cm^3] (Fig. 8) is probably reached, but due to lack of data at higher fluences, it remains open if the density really became independent of the fluence. The density obtained by combining our swelling data with the ion range from SRIM calculations is consistent with findings in earlier studies. For example, Bosia *et al.*[22] conclude that in their implantation experiments (500 keV He), a vacancy density of 4×10^{22} cm^{-3} is associated with a mass density of about 2.2 g/cm^3. This is similar to our results, where a vacancy densities of $1–2 \times 10^{23}$ cm^{-3} yields a mass density of 2.2–2.0 g/cm^3. However, these are values averaged over the whole irradiated volume with a thickness of 1.75 μm.

Electrical resistivity was measured for the irradiated samples and correlated with the density calculated from swelling. The electrical resistivity decreases with decreasing density. Vance *et al.*[66] show a strong correlation between the electrical resistivity of neutron-irradiated diamonds and the relative density reduction of

TABLE V. XRR parameters obtained from fitting for single crystal samples SC Ib and SC CVD irradiated with 5.3×10^{14} ions/cm^2 (low fluence) and 2.4×10^{15} ions/cm^2 (high fluence).

Sample	Layer	Roughness σ (nm)	Layer thickness t (nm)	Electron density ρ_e [e^-/Å^3]
SC Ib (Low fluence)	Surface	0	0.1(2)	0.16(5)
	Layer 1	1.8(1)	4.2(2)	0.82(5)
	Diamond	0.7(1)		1.03(5)
SC CVD (Low fluence)	Surface	0	0.3(2)	0.14(5)
	Layer 1	1.9(1)	4.8(2)	0.82(5)
	Diamond	0.8(1)		1.08(5)
SC Ib (High fluence)	Surface	0.4(1)	3.9(2)	0.16(5)
	Layer 2	1.5(1)	13.3(2)	0.41(5)
	Layer 1	1.7(1)	7.8(2)	1.03(5)
	Diamond	1.6(1)		1.08(5)
SC CVD (High fluence)	Surface	0.8(1)	1.2(2)	0.16(5)
	Layer 2	3.0(1)	7.5(2)	0.73(5)
	Layer 1	0.6(1)	1.5(2)	0.97(5)
	Diamond	1.2(1)		1.20(5)

the samples. They observed a decrease in resistivity over several orders of magnitude with decreasing density. For a density reduced by 45%, they observed an average resistivity of 0.3 Ω cm. The values for our ion-irradiated samples agree well with the data of Vance*et al.*.[66] Figure 11 shows that the resistivity decreases exponentially with the relative density change. These results support the densities calculated from the swelling.

As expected, the Raman spectra of the irradiated samples differ significantly from the spectra observed for the pristine samples. The spectra observed here are generally quite similar to those measured after irradiation of diamond with mega-electron volt alpha particles,[15] He ions (3.5 MeV),[14] (24–350 keV),[24] 130 MeV Xe and 112 MeV Kr ions,[26] 9 MeV B ions,[31] and fast neutrons.[26,68]

Three broad maxima were observed, and the two maxima in the region of 1000–1700 cm^{-1} were decomposed into Gaussians. A decomposition of the broad maximum at ≈1600 cm^{-1} (maximum III in Fig. 15) into two components yields one component with an energy of ≈1540 cm^{-1}. This is typical for Raman scattering of sp^3-bonded amorphous carbon (e.g., Prawer *et al.*[14]). The second component is centered around 1620 cm^{-1}. In a Raman spectroscopic study by Orwa *et al.*,[15] a prominent peak with, depending on the damage, a Raman shift between 1636 and 1616 cm^{-1} is observed. This peak is ascribed to the presence of C=C double bonds. The intensity of this peak is expected to be essentially independent of damage once a threshold of about 10^{22} vacancies/cm^3 has been exceeded. For high damages, a FWHM of 55 cm^{-1} is reported,[15] in agreement with our finding.

The decomposition of the broad maximum at ≈ 1250 cm^{-1} (maximum II in Fig. 15) into three components yields one component with an energy of 1280–1290 cm^{-1} and a FWHM of 90 cm^{-1}. This is the expected position and width of the first-order diamond line in irradiation-damaged diamond.[15] Orwa *et al.* showed that there is a near-linear increase of the FWHM of the first-order diamond line with the redshift of the peak position due to irradiation damage, and for the Raman band at 1296 cm^{-1}, they obtained a FWHM of ≈90 cm^{-1}, i.e., very close to the values we obtained here. They associated the shift from 1333 to 1296 cm^{-1} with the formation

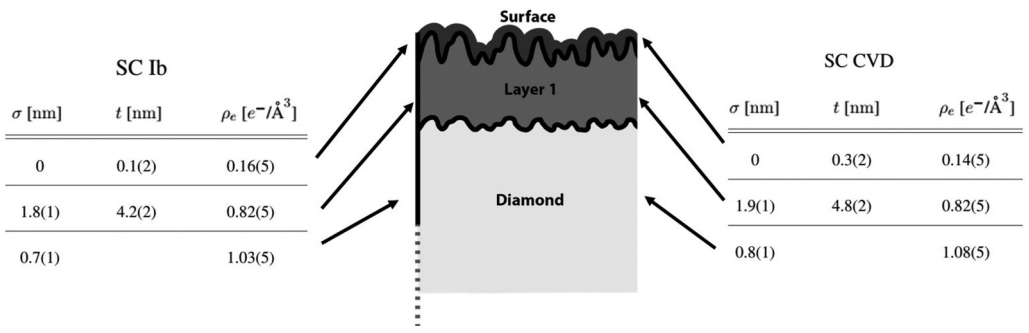

FIG. 19. Schematic of the layers fitted for sample SC Ib and SC CVD (low fluence) together with the obtained parameters. With σ = Roughness, t = Layer thickness, ρ_e = Electron density.

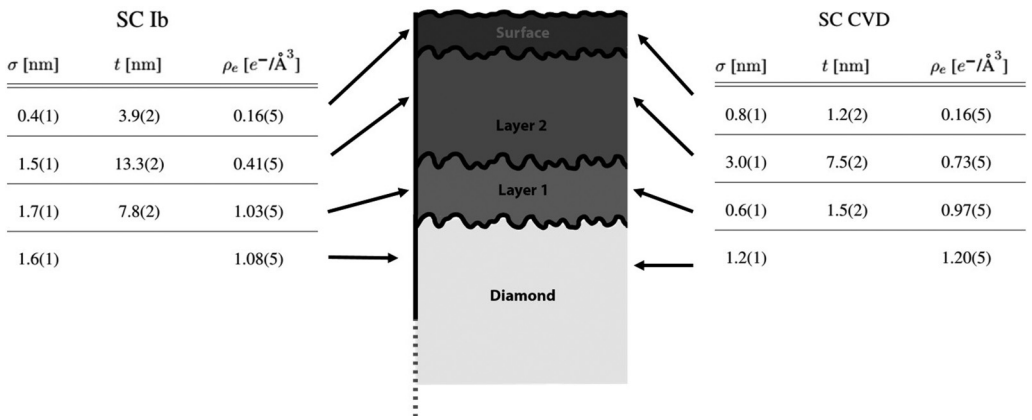

FIG. 20. Schematic of the layers fitted for sample SC Ib and SC CVD (high fluence) together with the obtained parameters. With σ = Roughness, t = Layer thickness, ρ_e = Electron density.

of $\approx 1.1 \times 10^{23}$ vacancies per cm^3, which is close to the damage we introduced into our diamonds (Fig. 3). We, therefore, conclude that this component is the redshifted and broadened first-order diamond line. The second component is centered at $\approx 1200\,\mathrm{cm}^{-1}$. From theory and experiment, Prawer *et al.*[14] concluded that this spectral feature is due to sp^3-bonded "amorphous diamond," i.e., severly damaged diamond with significant short range ordering. This is illustrated in Fig. 14, where a superposition of a Raman spectrum of an irradiation-damaged diamond, and a theoretical phonon density of states is shown. It has been discussed that defects induced by irradiation lead to the relaxation of selection rules (e.g., Khomich *et al.*[68]). We observe some correspondence between maxima in the DFT calculated pDOS and the experimentally determined Raman spectrum. The same argument holds for the third component at $\approx 1120\,\mathrm{cm}^{-1}$, which also coincides with a further distinct maximum in the pDOS. The origin of the often observed maximum at $\approx 350\,\mathrm{cm}^{-1}$ cannot be directly associated with a maximum in the phonon density of states. However, based on a simple oscillator model, the appearance of Raman scattering in the irradiated sample above the highest frequency mode of diamond implies the formation of stronger bonds such as C=C double bonds.

Raman spectroscopy, however, also probes a comparatively large sample volume, and the Raman signal is a superposition of scattering contributions from a typical depth of the order of micrometers into the sample. In the present case, the incident laser light has to transverse a nearly opaque layer and any scattered photons also have to pass through this layer before reaching the detector. This is the most likely explanation for the absence of a sharp Raman diamond line due to unperturbed diamond present below the irradiated volume.

According to our XRR analysis, the irradiation with 14 MeV Au^{6+} ions, leads to the formation of subsurface layers of reduced density. For the samples irradiated with the low fluence (5.3×10^{14} ions/cm^2), the subsurface layer has a thickness of 4–5 nm, which increases to about 10–20 nm at a fluence of 2.4×10^{15} ions/cm^2 and can only be modeled by adding an

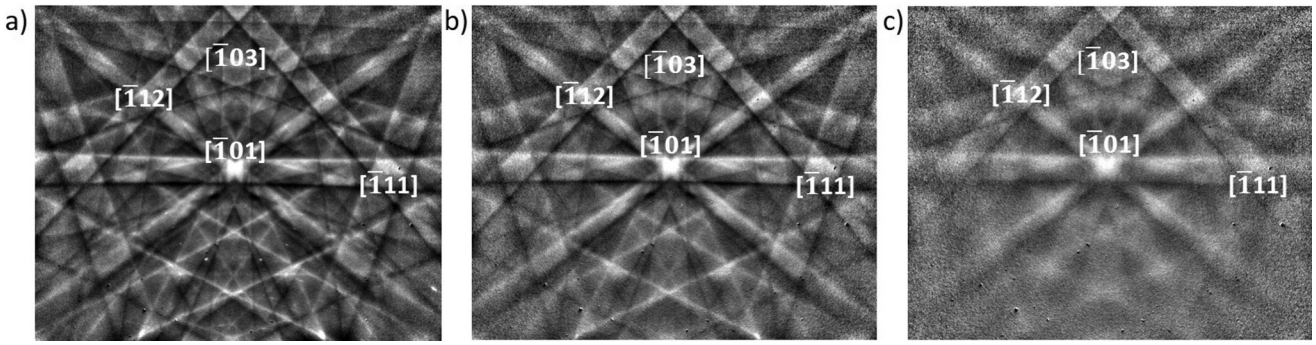

FIG. 21. Electron backscatter patterns collected with the EBSD camera for a single crystal diamond sample SC Ib. (a) Pristine diamond, (b) diamond irradiated with a low fluence (1.8×10^{15} ions/cm^2), and (c) diamond irradiated with a high fluence (2.4×10^{15} ions/cm^2).

additional low-density layer. The fits to the XRR data conclusively show that, irrespective of the details, the thickness of the subsurface region which is severely damaged strongly depends on the fluence.

Markwitz *et al.*[70] investigated the changes of alternating deposited Al - Au multilayers upon MeV He^+ ion irradiation with XRR. The authors observed a significant decrease in density in the near-surface region, an increase in surface roughness, and the appearance of an ultra thin layer at the surface, with significantly reduced density compared to the underlying layers. This layer increases in thickness after irradiation. Markwitz *et al.*[70] conclude this ultra thin layer to be due to the influence of light element impurities, mainly hydrogen and oxygen on the near-surface region. Stachura *et al.*[71] investigated deposited titanium oxide nanolayers irradiated with low-energy highly charged Xe ions with XRR. The authors found that the density and thickness of the top layer slightly changes only for the sample irradiated with highly charged Xe ions. The density of the layer decreased, while the thickness increased. They suggest amorphization of the top layer. However, the layers described by Markwitz *et al.*[70] and Stachura *et al.*[71] were deposited on substrates before irradiation, unlike the modified layers in our experiments. We also observed an ultra thin layer at the surface with a significant reduced density. The thickness of the layer increases with increasing fluence.

The results from XRR clearly show layered, highly damaged surfaces for the ion-irradiated diamonds. The densities of the surfaces are significantly reduced, which indicates an amorphization of the first 5–20 nm of the samples. The densities of the layers imply that the produced damage has its maximum close to the surface and decreases with sample depth until a significantly less damaged material with the density of diamond is observed.

The surface roughness was measured by AFM. For both single crystal samples, the irradiation caused a noticeable surface roughening. It seems that higher fluences lead to slightly less surface roughening, but there are too few data points to conclude this reliably. Comparing the roughness from AFM ($50 \times 50\,\mu m^2$) and XRR measurements ($0.7 \times 0.03\,mm^2$), we find similar values in the order of 1–5 nm. For the irradiated samples, the AFM data show a roughness increase by a factor of ≈2–3. The results from AFM support the XRR data, which imply that the irradiated surface and the immediate subsurface are strongly modified. A direct comparison with the AFM data is not possible, as the XRR data are fitted with a complex layer model, which cannot be easily interpreted in terms of the surface topology.

The finding from the analysis of the XRR data is further supported by the observation of a significant decrease in the quality of electron backscatter patterns on irradiation. Winkelmann[69] concluded that for EBSD studies of silicon with a primary beam energy of 20 kV the measured diffraction pattern reflects the atomic arrangement of the first few tens of nanometers. With EBSD, we were not able to distinguish whether the damage is homogenous in the volume illuminated by the electron beam or whether we have a layered structure with more damage closer to the surface and less damage deeper in the sample.

We have to reconcile the observation that swelling and decreased resistivity implies the presence of material with an average density of 2.0–2.9 g/cm^3, depending on the irradiation fluence. The only model fitting all of these observations is that there is a highly damaged buried layer with strongly reduced density due to ion stopping at ≈1.75 μm depth. Above this layer, the structural damage must decrease continuously (and the density correspondingly increase) toward the surface so that a few tens of nanometers below the surface there is only slightly damaged diamond with a density close to that of pristine diamond, and the ability to cause constructive interference in diffracted electrons but with enough defects to substantially shift and broaden the first-order diamond Raman line. The top 5–20 nm are then highly damaged.

V. SUMMARY

The densities (deduced from our swelling data) are all below the critical density for amorphization given by Fairchild *et al.*[21] For the highest applied fluence (2.4×10^{15} ions/cm^2), the damage saturation value suggested by Fairchild *et al.*[21] was probably reached. Electrical resistivity was measured for the irradiated samples. An exponential decrease in electrical resistivity with decreasing density is observed, and the results support the densities calculated from the swelling. With Raman spectroscopy, we clearly observe the well-defined significant shift and the broadening of the diamond line and the spectroscopic signatures of amorphous sp^3 carbon and structural modifications, such as the formation of C═C double bonds due to irradiation.

XRR provides clear evidence of highly damaged surfaces and the formation of subsurface layers of reduced density upon irradiation. The layers increase in number and thickness with increasing fluence. The significantly reduced density indicates the amorphization of the samples surface. The observed densities imply that the damage has its maximum close to the surface and decreases with sample depth. These findings are supported by the observation of a significant decrease of the quality of electron backscatter patterns on irradiation. An increased surface roughness due to irradiation was further measured by AFM.

In summary, by a combination of complementary characterization techniques, we have shown that the ion-irradiation induced changes to the surface and subsurface of diamonds are rather complex. By studying differently doped single crystal and polycrystalline samples, we showed that these changes are independent of the doping and microstructure of the samples. Specifically, the radiation damage in the first few nanometers is much more severe than at greater depths and so far not predicted by model calculations. We expect that the damage close to the surface has a strong influence on any surface process such as etching. Based on our existing data set, it is not clear if continued irradiation will lead to an extension of the highly damaged top layer. Further experiments are needed to clarify how the structure and density of the first few tens of nanometers evolve under more extensive ion irradiations.

ACKNOWLEDGMENTS

This work has been funded via the R&D program of GSI Helmholtzzentrum für Schwerionenforschung. B.W. is grateful for support by the BIOVIA Science Ambassador program and support by the BMBF Project No. 02NUK060E. I.A. acknowledges financial support by CAPES Grant Nos. 88887.176042/2018-00 and 88882.314866/2019-01 as well as auspices by Instituto Nacional de Engenharia de Superfície (INES, Brazil). W.M. acknowledges

financial support by BMBF funded Project (Nos. 05K19IP2 and 05K16RFB). The authors are grateful to the operation staff of the Tandetron accelerator at UFRGS (Porto Alegre, Brazil) for providing excellent ion beam conditions. The accelerator is financially supported by CAPES (Finance Code 001). We acknowledge DESY (Hamburg, Germany), a member of the Helmholtz Association HGF, for the provision of experimental facilities. Part of this research was carried out at PETRA III beamline P08. We would further like to acknowledge and thank Professor Michael Huth (Institute of Physics, Goethe University Frankfurt) for providing access to the AFM and Professor Horst Marschall (Institute of Geosciences, Goethe University Frankfurt) for providing access to the Keyence digital microscope.

DATA AVAILABILITY

The data that support the findings of this study are available from the corresponding author upon reasonable request.

REFERENCES

[1]A. M. Zaitsev, *Optical Properties of Diamond: a Data Handbook* (Springer Science & Business Media, 2013).
[2]R. Balmer, I. Friel, S. Woollard, C. Wort, G. Scarsbrook, S. Coe, H. El-Hajj, A. Kaiser, A. Denisenko, E. Kohn *et al.*, Philos. Trans. R. Soc. A **366**, 251 (2008).
[3]M. Kasu, K. Ueda, Y. Yamauchi, A. Tallaire, and T. Makimoto, Diam. Relat. Mater. **16**, 1010–1015 (2007).
[4]J. Park, V. Quaiserová-Mocko, B. A. Patel, M. Novotnỳ, A. Liu, X. Bian, J. J. Galligan, and G. M. Swain, Analyst **133**, 17 (2008).
[5]B. Campbell, W. Choudhury, A. Mainwood, M. Newton, and G. Davies, Nucl. Inst. Methods Phys. Res. Sect. A **476**, 680 (2002).
[6]E. Bossini and N. Minafra, Front. Phys. **8**, 248 (2020).
[7]R. Tapper, Rep. Progress Phys. **63**, 1273 (2000).
[8]J. Prins, T. Derry, and J. Sellschop, Phys. Rev. B **34**, 8870 (1986).
[9]M. Wong, F. Karioris, L. Cartz, and E. Vance, Radiat. Eff. **104**, 99 (1987).
[10]J. F. Prins, Mater. Sci. Rep. **7**, 275 (1992).
[11]R. Kalish and S. Prawer, Nucl. Inst. Methods Phys. Res. Sect. B **106**, 492 (1995).
[12]S. Prawer and R. Kalish, Phys. Rev. B **51**, 015711 (1995).
[13]C. Uzan-Saguy, C. Cytermann, R. Brener, V. Richter, M. Shaanan, and R. Kalish, Appl. Phys. Lett. **67**, 1194 (1995).
[14]S. Prawer, K. Nugent, and D. Jamieson, Diam. Relat. Mater. **7**, 106 (1998).
[15]J. Orwa, K. Nugent, D. Jamieson, and S. Prawer, Phys. Rev. B **62**, 5461 (2000).
[16]R. Kalish, *Semiconductors and Semimetals* (Elsevier, 2003), Vol. 76, p. 145.
[17]R. Brunetto, G. A. Baratta, and G. Strazzulla, J. Phys. Conf. Seri. **6**, 120 (2005).
[18]D. Hickey, K. Jones, and R. Elliman, Diam. Relat. Mater. **18**, 1353 (2009).
[19]F. Bosia, S. Calusi, L. Giuntini, S. Lagomarsino, A. L. Giudice, M. Massi, P. Olivero, F. Picollo, S. Sciortino, A. Sordini *et al.*, Nucl. Inst. Methods Phys. Res. Sect. B **268**, 2991 (2010).
[20]F. Bosia, N. Argiolas, M. Bazzan, P. Olivero, F. Picollo, A. Sordini, M. Vannoni, and E. Vittone, Diam. Relat. Mater. **20**, 774 (2011).
[21]B. A. Fairchild, S. Rubanov, D. W. Lau, M. Robinson, I. Suarez-Martinez, N. Marks, A. D. Greentree, D. McCulloch, and S. Prawer, Adv. Mater. **24**, 2024 (2012).
[22]F. Bosia, N. Argiolas, M. Bazzan, B. A. Fairchild, A. D. Greentree, D. W. Lau, P. Olivero, F. Picollo, S. Rubanov, and S. Prawer, J. Phys.: Condens. Matter **25**, 385403 (2013).
[23]S.-S. Chen, H.-C. Chen, W.-C. Wang, C.-Y. Lee, I.-N. Lin, J. Guo, and C.-L. Chang, J. Appl. Phys. **113**, 113704 (2013).
[24]R. Khmelnitsky, V. Dravin, A. Tal, M. Latushko, A. Khomich, A. Khomich, A. Trushin, A. Alekseev, and S. Terentiev, Nucl. Inst. Methods Phys. Res. Sect. B **304**, 5 (2013).
[25]J. Schwartz, S. Aloni, D. Ogletree, M. Tomut, M. Bender, D. Severin, C. Trautmann, I. Rangelow, and T. Schenkel, J. Appl. Phys. **116**, 214107 (2014).
[26]O. Poklonskaya, S. Vyrko, A. Khomich, A. Averin, A. Khomich, R. Khmelnitsky, and N. Poklonskia, J. Appl. Spectrosc. **81**, 969 (2015).
[27]G. García, M. Díaz-Híjar, V. Tormo-Márquez, I. Preda, O. Peña-Rodríguez, and J. Olivares, Diam. Relat. Mater. **58**, 226 (2015).
[28]R. A. Khmelnitsky, V. A. Dravin, A. A. Tal, E. V. Zavedeev, A. A. Khomich, A. V. Khomich, A. A. Alekseev, and S. A. Terentiev, J. Mater. Res. **30**, 1583 (2015).
[29]G. García, I. Preda, M. Díaz-Híjar, V. Tormo-Márquez, O. Peña-Rodríguez, J. Olivares, F. Bosia, N. Pugno, F. Picollo, L. Giuntini *et al.*, Diam. Relat. Mater. **69**, 1 (2016).
[30]F. Agulló-Rueda, N. Gordillo, M. Ynsa, A. Maira, J. Cañas, and M. Ramos, Carbon **123**, 334 (2017).
[31]F. Agulló-Rueda, M. Ynsa, N. Gordillo, A. Maira, D. Moreno-Cerrada, and M. Ramos, Diam. Relat. Mater. **72**, 94 (2017).
[32]V. Anikin, A. Borisov, V. Kazakov, A. Kudrin, E. Mashkova, A. Morkovkin, M. Ovchinnikov, and E. Pitirimova, J. Surf. Invest. **12**, 801 (2018).
[33]J. Lindhard, M. Scharff, and H. E. Schiøtt, *Range Concepts and Heavy ion Ranges* (Munksgaard Copenhagen, 1963).
[34]J. Ziegler, Appl. Phys. Lett. **31**, 544 (1977).
[35]J. F. Ziegler and J. P. Biersack, *Treatise on Heavy-ion Science* (Springer, 1985), p. 93.
[36]M. Dresselhaus, R. Kalish, and J. F. Prins, Phys. Today **46**, 65 (1993).
[37]A. Johannes, H. Holland-Moritz, and C. Ronning, Semicond. Sci. Technol. **30**, 033001 (2015).
[38]R. E. Stoller, M. B. Toloczko, G. S. Was, A. G. Certain, S. Dwaraknath, and F. A. Garner, Nucl. Inst. Methods Phys. Res. Sect. B **310**, 75–80 (2013).
[39]K. Nordlund, S. J. Zinkle, A. E. Sand, F. Granberg, R. S. Averback, R. E. Stoller, T. Suzudo, L. Malerba, F. Banhart, W. J. Weber *et al.*, J. Nucl. Mater. **512**, 450 (2018).
[40]H. Amekura and N. Kishimoto, J. Appl. Phys. **104**, 063509 (2008).
[41]H. O. Pierson, *Handbook of Carbon, Graphite, Diamonds and Fullerenes: Processing, Properties and Applications* (William Andrew, 2012).
[42]G. Binnig, C. F. Quate, and C. Gerber, Phys. Rev. Lett. **56**, 930 (1986).
[43]A. C. Ferrari and J. Robertson, Philos. Trans. R. Soc. Lond. Ser. A **362**, 2477 (2004).
[44]J. Daillant and A. Gibaud, *X-ray and Neutron Reflectivity: Principles and Applications* (Springer, 2008), Vol. 770.
[45]A. J. Schwartz, M. Kumar, B. L. Adams, and D. P. Field, *Electron Backscatter Diffraction in Materials Science* (Springer, 2009), Vol. 2.
[46]See https://www.e6.com/de/ for "Element Six Synthetic Industrial Diamonds" (2020).
[47]R. Balmer, J. Brandon, S. Clewes, H. Dhillon, J. Dodson, I. Friel, P. Inglis, T. Madgwick, M. Markham, T. Mollart *et al.*, J. Phys.: Condens. Matter **21**, 364221 (2009).
[48]J. Ziegler, J. Biersack, and M. Ziegler, See http://www.srim.org for "SRIM: The Stopping and Range of Ions in Matter, Version SRIM-2013".
[49]W. J. Weber and Y. Zhang, Curr. Opin. Solid State Mater. Sci. **23**, 100757 (2019).
[50]J. Koike, D. Parkin, and T. Mitchell, Appl. Phys. Lett. **60**, 1450 (1992).
[51]D. P. Woodruff, *Modern Techniques of Surface Science* (Cambridge University Press, 2016).
[52]D. Nečas and P. Klapetek, Cent. Eur. J. Phys. **10**, 181 (2012).
[53]H. Topsoe, Bulletin **472**(13), 63 (1968).
[54]L. Bayarjargal, C.-J. Fruhner, N. Schrodt, and B. Winkler, Phys. Earth Planet. Interiors **281**, 31 (2018).
[55]P. Hohenberg and W. Kohn, Phys. Rev. **136**, B864 (1964).
[56]J. P. Perdew, K. Burke, and M. Ernzerhof, Phys. Rev. Lett. **77**, 3865 (1996).
[57]S. J. Clark, M. D. Segall, C. J. Pickard, P. J. Hasnip, M. I. J. Probert, K. Refson, and M. C. Payne, Z. Kristallogr. **220**, 567 (2005).
[58]K. Lejaeghere, G. Bihlmayer, T. Björkman, P. Blaha, S. Blügel, V. Blum, D. Caliste, I. E. Castelli, S. J. Clark, D. Corso *et al.*, Science **351**, aad3000 (2016).

[59]H. J. Monkhorst and J. D. Pack, Phys. Rev. B **13**, 5188 (1976).
[60]K. Miwa, Phys. Rev. B **84**, 094304 (2011).
[61]H. Kiessig, Ann. Phys. **402**, 769 (1931).
[62]G. Vignaud and A. Gibaud, J. Appl. Crystallogr. **52**, 201 (2019).
[63]J. A. Nelder and R. Mead, Comput. J. **7**, 308 (1965).
[64]R. A. Schwarzer, D. P. Field, B. L. Adams, M. Kumar, and A. J. Schwartz, *Electron Backscatter Diffraction in Materials Science* (Springer, 2009), p. 1.
[65]Oxford Instruments, "Aztec Manual" (2021).
[66]E. R. Vance, H. J. Milledge, and A. T. Collins, J. Phys. D: Appl. Phys. **5**, L40 (1972).
[67]V. Mortet, A. Taylor, Z. V. Živcová, D. Machon, O. Frank, P. Hubík, D. Trémouilles, and L. Kavan, Diam. Relat. Mater. **88**, 163 (2018).
[68]A. A. Khomich, R. A. Khmelnitsky, and A. V. Khomich, Nanomaterials **10**, 1166 (2020).
[69]A. Winkelmann, J. Microsc. **239**, 32 (2010).
[70]A. Markwitz, F. Prokert, M. Waldschmidt, and G. Demortier, Nucl. Inst. Methods Phys. Res. Sect. B **143**, 422–426 (1998).
[71]R. Stachura, A. Kubala-Kukuś, D. Banaś, I. Stabrawa, K. Szary, P. Jagodziński, G. Aquilanti, I. B. Mihalić, M. Pajek, J. Semaniak *et al.*, Acta Phys. Polonica A **137**, 38–43 (2020).